ACS APPLIED NANO MATERIALS
Cite This: ACS Appl. Nano Mater. 2018, 1, 2143−2152
Article
www.acsanm.org

Engineering Molybdenum Diselenide and Its Reduced Graphene Oxide Hybrids for Efficient Electrocatalytic Hydrogen Evolution

Swagotom Sarker,[†] Jonathan Peters,[†] Xinqi Chen,[‡] Binsong Li,[∥] Gen Chen,[†] Litao Yan,[†] Stephanie K. Richins,[†] Sanjib Das,[§] Meng Zhou,[†] and Hongmei Luo*[,†]

[†]Department of Chemical and Materials Engineering, New Mexico State University, Las Cruces, New Mexico 88003, United States
[‡]Northwestern University Atomic and Nanoscale Characterization Experimental (NUANCE) Center and [§]Department of Materials Science and Engineering, Northwestern University, Evanston, Illinois 60208, United States
[∥]Tsinghua Innovation Center in Dongguan, Building 8, Sci& Tech. Innovation Park, Songshan Lake National High-Tech Industrial Development Zone, Dongguan, Guangdong 523808, P. R. China

Supporting Information

ABSTRACT: We report the hydrogen evolution reaction (HER) with molybdenum diselenide ($MoSe_2$) and its reduced graphene oxide (rGO) hybrids synthesized by a microwave process followed by annealing at 400 °C. The content of GO was varied to understand its role in the electrocatalytic activities. Electrochemical performance of the as-synthesized and the annealed catalysts underscores (i) a requirement of catalytic activation of the as-synthesized samples, (ii) an apparent shift in the onset potential as a result of annealing, and (iii) striking changes in the Tafel slope as well as the overpotential. The results clearly reveal that partially crystalline plain $MoSe_2$ is more elctroactive in comparison to its annealed counterpart, whereas annealing is advantageous to $MoSe_2$/rGO. Improved HER performances of the annealed $MoSe_2$/rGO hydrids arise from the synergistic effect between active $MoSe_2$ and rGO of improved conductivity. The annealed hybrid of $MoSe_2$ with rGO designated as $MoSe_2$/rGO100_400 °C demonstrated an excellent HER activity with a small onset potential of −46 mV vs reversible hydrogen electrode, a smaller Tafel slope (61 mV/dec), and a reduced overpotential of 186 mV at −10 mA/cm^2. As a result of a convenient synthetic process and the suitable electrocatalytic performance, this study would be beneficial to designing and fabricating other nanomaterials with/without a conductive support for their versatile applications.

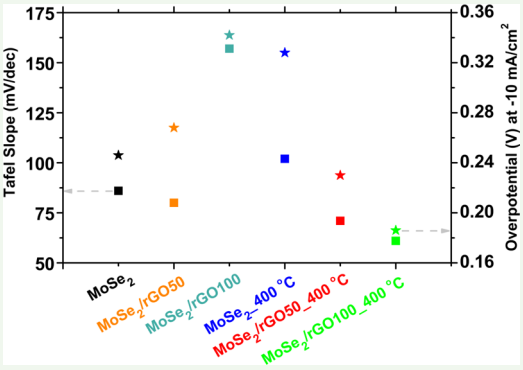

KEYWORDS: *microwave, $MoSe_2$, reduced graphene oxide, annealing, electrocatalytic hydrogen evolution*

INTRODUCTION

Increase in global energy demand and concern over environmental sustainability for a better future have generated awareness for innovation under the hydrogen economy paradigm.[1,2] Hydrogen, a zero emission clean energy carrier, can be produced by both photocatalysis[3,4] and (photo)-electrocatalysis.[5,6] Water electrocatalysis is one of the most promising processes to produce hydrogen, and its efficiency significantly depends on the catalysts used for the hydrogen evolution reaction (HER).[7−11] The criterion that dominates to determine the effectiveness of the catalysts is the requirement of low overpotential at high current density.[12,9] The Gibbs free energy of an optimal HER catalyst should approximately be zero (e.g., $\Delta G_H^\circ \approx 0$) for the adsorbed hydrogen on the catalyst sites, and as a result, platinum (Pt) and its alloys are considered as the best catalysts.[9,13] However, high cost and scarcity of Pt limit the wider applications for water electrocatalysis. As a result, the development of the potential catalysts from various earth abundant transitional metals[14] and their dichalcogenides, phosphide, carbide such as MoS_2,[13,15] $MoSe_2$,[9,16] CoP,[17] and Mo_2C[18,19] have generated much research interest. Among them from theoretical[20] and experimental[21] perspectives, reports on 2D transition metal dichalcogenides (TMDCs) are predominant, and they exhibit excellent HER activity in the acidic media. For example, MoS_2 demonstrates high electrocatalytic performance and good durability.[13,15] Both theoretical and experimental studies highlight that the HER activity of the TMDCs depends closely on the active sites, which are essentially located at the edges as well as the defects,[22] and the basal plane is catalytically inert.[15,23,24] However, their applications are restricted by layer stacking and agglomeration, i.e., reduction of catalytic sites, low conductivity among the TMDC layers bonded by the van der Waals force,[25] and poor charge transport between current collector and TMDCs.[9] In response to these deficiencies to improve the HER performance, several synthesis protocols such as hydrothermal/

Received: February 7, 2018
Accepted: April 18, 2018
Published: April 18, 2018

DOI: 10.1021/acsanm.8b00208
ACS Appl. Nano Mater. 2018, 1, 2143−2152

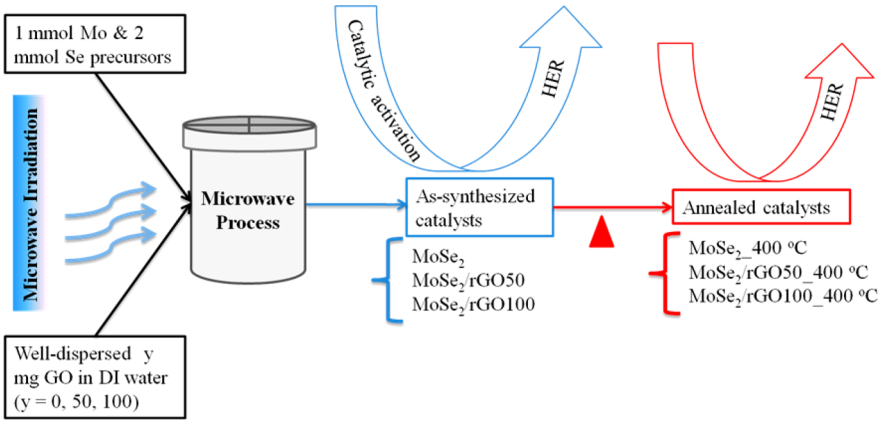

Figure 1. Schematic illustration of the preparation of various catalysts and the electrocatalysis.

solvothermal,[9,26] chemical vapor deposition,[27] and electrodeposition[28,29] have been reported for various TMDCs. Moreover, improved charge transport and exposure of more catalytic sites in dichalcogenides are mostly realized by the preservation of the nanostructure,[30] the doping,[31] and the incorporation of various conductive supports such as graphene[9,32,33] and carbon nanotubes.[34] HER studies using doped structures (MoS_2, $MoSe_2$),[31,35] WS_2/graphene,[36] MoS_2/graphene,[37] MoS_2/carbon nanotubes,[38] $MoSe_2$/graphene,[9] $MoSe_2$/carbon fiber,[39] and $MoSe_2$/cotton[40] have been reported. It is interesting to observe that among the wide range reports on TMDC electrocatalysts, there have been a few studies on both $MoSe_2$ and its graphene nanohybrids unlike MoS_2 and its graphene hybrids for HER. $MoSe_2$, which possesses relatively higher conductivity and narrower bandgap than those of MoS_2, is considered as a superior electrocatalyst.[9,30] Li et al.[41] and Ekspong et al.[42] suggested that low crystalline quality of molybdenum sulfide is likely to be superior toward achieving low Tafel slopes. Utilizing plasma-enhanced chemical vapor deposition (PECVD), Mao et al. fabricated perpendicularly oriented $MoSe_2$ nanosheets over 3D graphene network, which exhibited an outstanding HER activity.[30] Yang's group designed $MoSe_2$/graphene hybrid using the hydrothermal method, and it showed improved HER performance.[9] Moreover, computational study validated the requirement of lower Gibbs free energy on the selenided Mo edges of $MoSe_2$.[9,20,43] Therefore, interest lies in understanding experimental conditions to enhance the catalytic activities of $MoSe_2$. To the best of our knowledge, catalytic activation and engineering of a simple microwave process assisted synthesis of $MoSe_2$ and its reduced graphene oxide (rGO) hybrids via the transformation of composition, crystallinity, and conductivity which is yet to be reported to discern efficient hydrogen evolution reaction.

Herein, we utilized a one-pot microwave process to synthesize $MoSe_2$ and its hybrids with rGO. The impact of annealing of the as-synthesized samples was realized from a comparative study on electrocatalytic hydrogen evolution. The overall process is illustrated in Figure 1. Although this microwave process consisted of a very short span of time, distinct few layered $MoSe_2$ can easily be incorporated with rGO. With the help of various characterizations, the HER study revealed that (i) as-synthesized partially crystalline $MoSe_2$ transformed into an actual HER catalyst, (ii) the incorporation of rGO with $MoSe_2$ in the hybrids influenced the HER activity, and (iii) electrocatalytic performance significantly changed owing to annealing of the as-synthesized samples. It was observed that annealed $MoSe_2$ with rGO demonstrated smaller Tafel slopes and reduced overpotentials in comparison to their as-synthesized counterparts. However, annealing negatively impacted the performance of plain $MoSe_2$. The results indicated that the simple microwave process could be used to fabricate various electroactive materials, and the comparative analysis of the HER performance would be supportive to realize for other electrocatalytic studies.

EXPERIMENTAL DETAILS

Materials. The following chemicals were purchased from Sigma-Aldrich: sodium molybdate dihydrate ($Na_2MoO_4{\cdot}2H_2O$, ≥99.5%), selenium (Se, 99.999%, mesh −100), hydrazine monohydrate ($N_2H_4{\cdot}H_2O$, 64−65%, reagent grade 98%), sodium nitrate ($NaNO_3$, ≥99%), sulfuric acid (H_2SO_4, 95−98%), potassium permanganate ($KMnO_4$, ≥99%), hydrogen peroxide (H_2O_2, 30 wt % in water), hydrochloric acid (HCl, 37%), and nafion 117 solution. Graphite powder (99.9%), commercial 20 wt % platinum on carbon (Pt/C), and ethanol (absolute, anhydrous) were obtained from Alfa-Aesar, Fuel Cell Store, and Pharmco-Aaper, respectively. The above chemicals were used without further purification.

Synthesis of $MoSe_2$ and Its Reduced Graphene Oxide Hybrids. $MoSe_2$ and its rGO hybrids were synthesized using a microwave hydrothermal process followed by annealing under argon gas flow. First, graphene oxide (GO) was prepared via the modified Hummers method.[44,45] In a typical synthesis for $MoSe_2$/rGO hybrid, 100 mg of GO was dispersed in 18 mL of DI water, and 1 mmol of $Na_2MoO_4{\cdot}2H_2O$ was dissolved in it under magnetic stirring for 30 min. 2 mmol of Se powder was dissolved in 9 mL of $N_2H_4.H_2O$ solution in a separate flask at room temperature. Then, it was mixed with the solution of $Na_2MoO_4{\cdot}2H_2O$ and GO. The mixture was transferred to a 45 mL Teflon-lined microwave reactor (Model 4782, Parr Instrument) and properly tightened. The reactor was placed under the microwave irradiation (Panasonic NN-SD972S 1250 W microwave) at 375 W for 3 min and 30 s and allowed to cool to room temperature after irradiation. Synthesized material was thoroughly washed and collected by performing vacuum filtration with DI water and methanol. The collected material was vacuum-dried at 70 °C overnight, and a fraction of the vacuum-dried sample was annealed at 400 °C for 3 h under argon gas flow to obtain the final products. Red selenium was found to deposit along the wall of the quartz tube in the downstream of the gas flow during annealing. The as-synthesized sample and its corresponding annealed product are designated as $MoSe_2$/rGO100 and $MoSe_2$/rGO100_400 °C, respectively. To understand the impact of the introduction of GO and annealing, $MoSe_2$/rGO50 and $MoSe_2$/rGO50_400 °C were also prepared using 50 mg of GO, while other process parameters were kept unchanged. Furthermore, as-synthesized $MoSe_2$ was also synthesized without the addition of GO under the same microwave process, and its annealed

DOI: 10.1021/acsanm.8b00208
ACS Appl. Nano Mater. 2018, 1, 2143−2152

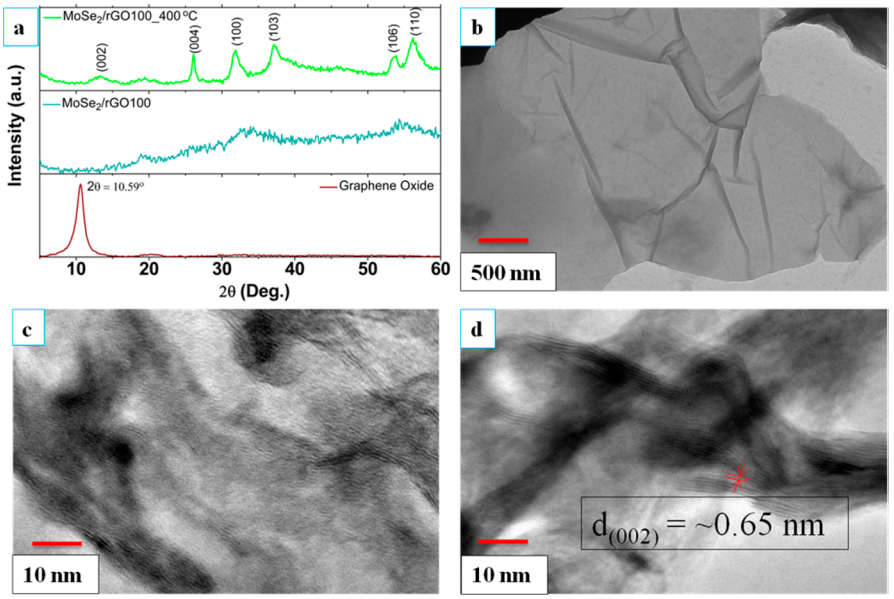

Figure 2. (a) XRD patterns of graphene oxide, $MoSe_2$/rGO100, and $MoSe_2$/rGO100_400 °C. TEM images of (b) graphene oxide, (c) $MoSe_2$/rGO100, and (d) $MoSe_2$/rGO100_400 °C.

component is denoted as $MoSe_2$_400 °C. *Note: $N_2H_4{\cdot}H_2O$ and Se should be handled very carefully.*

Materials Characterization. Transmission electron microscope (TEM) images were obtained using the H-7650 (Hitachi High-Technologies Corp., 80 kV) and the JEOL 2010 (200 kV). A Rigaku Miniflex-II diffractometer with Cu Kα radiation (λ = 1.5406 Å) at 30 kV and 15 mA was used to perform X-ray diffraction (XRD). Raman spectra were collected using a Reinshaw 2000 Raman microscope with 632.8 nm (1.96 eV) laser excitation. X-ray photoelectron spectroscopy (XPS) analysis was conducted with a Thermo Fisher ESCALAB 250Xi using the Al Kα X-ray source (1486.6 eV). The XPS spectra were calibrated against the adventitious carbon (C 1s) peak at 284.80 eV. Fourier transformed infrared (FTIR) spectra were collected using the PerkinElmer Frontier FTIR/NIR spectrometer.

Electrochemical Measurements. A typical working electrode preparation procedure is as follows. 5 mg of each sample ($MoSe_2$, $MoSe_2$_400 °C, $MoSe_2$/rGO50, $MoSe_2$/rGO50_400 °C, $MoSe_2$/rGO100, $MoSe_2$/rGO100_400 °C, and Pt/C) was dispersed in 1 mL of ethanol–nafion solution (950 μL of absolute ethanol:50 μL of nafion solution) and ultrasonicated for 30 min to prepare a homogeneous ink. A rotating disc glassy carbon electrode was polished using an alumina suspension (0.05 μm, Allied High Tech Products) for 30 min. Then, it was cleaned with DI water under ultrasonication and dried under air flow. 10 μL of catalyst ink was drop-casted on the glassy carbon electrode (area = 0.196 cm^2), resulting in a mass loading of ~0.253 mg/cm^2, and the catalyst ink incorporated electrode was air-dried prior to electrochemical measurements.

All electrochemical measurements for the hydrogen evolution reaction were performed under a typical three-electrode cell setup: electrocatalyst incorporated rotating disk glassy carbon electrode as the working electrode, Ag/AgCl (4 M KCl) as the reference electrode, and Pt coil as the counter electrode using a CHI 760C electrochemical workstation. 0.5 M H_2SO_4 was used as the electrolyte. The three-electrode potentials were converted into the reversible hydrogen electrode (RHE) potential utilizing the Nernst equation: $E_{RHE} = E_{Ag/AgCl} + 0.059pH + E^0_{Ag/AgCl}$, while the reference electrode was calibrated with hydrogen gas saturated 0.5 M H_2SO_4 (Figure S1). The rotational speed of the rotating disk glassy carbon electrode was maintained at 1000 rpm for all measurements. Linear sweep voltammetric (LSV) polarization curves were generated at 5 mV/s. Electrochemical impedance spectroscopy (EIS) measurements were carried out from 10^5 to 0.1 Hz at an overpotential of 205 mV and 5 mV of ac amplitude after catalytic activation. Electrocatalytic activities were analyzed with and without *iR* compensation. To evaluate stability, time-dependent current density (j–t) profiles were examined at a constant overpotential of 245 mV for 4000 s.

RESULTS AND DISCUSSION

Morphology and Surface Analyses. First, the prepared samples were characterized using XRD to inspect crystallinity.

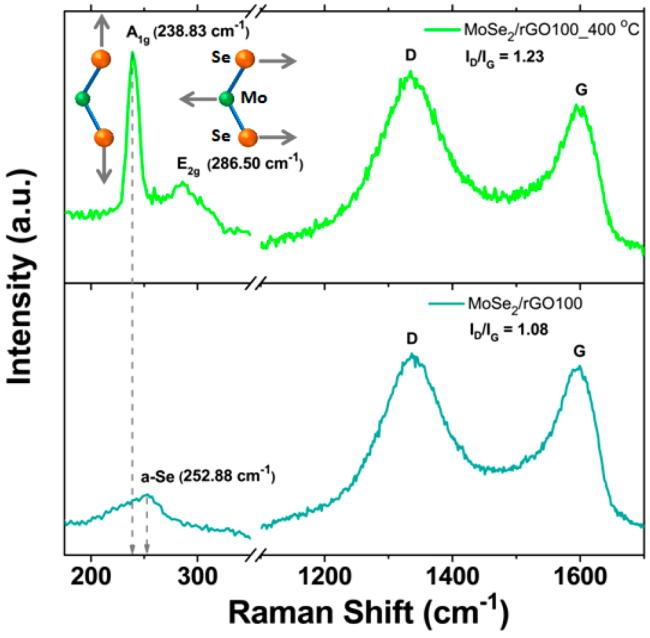

Figure 3. Raman spectra of $MoSe_2$/rGO100 and $MoSe_2$/rGO100_400 °C with illustration of atomic vibration of A_{1g} (left) and E^1_{2g} (right) as inserted.

Figure 2a presents the XRD patterns of GO, $MoSe_2$/rGO100, and $MoSe_2$/rGO100_400 °C. GO showed its characteristic peak at 2θ = 10.59°, which corresponds to (002) plane.[46] It is noteworthy that hydrazine also works as a reducing agent

DOI: 10.1021/acsanm.8b00208
ACS Appl. Nano Mater. 2018, 1, 2143–2152

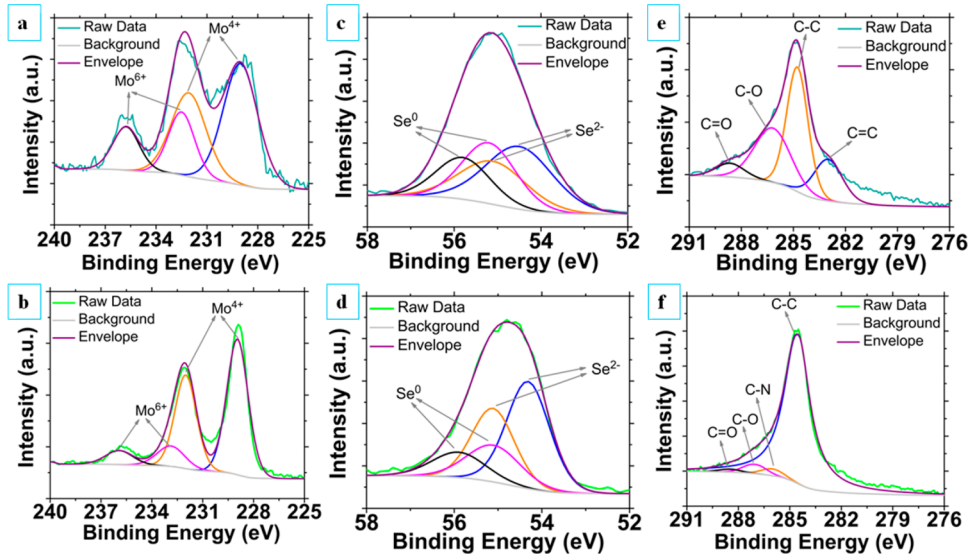

Figure 4. XPS spectra of (a) Mo 3d, (c) Se 3d, and (e) C 1s in $MoSe_2$/rGO100 (first row). Corresponding XPS spectra of (b) Mo 3d, (d) Se 3d, and (f) C 1s in $MoSe_2$/rGO100_400 °C presented in the second row.

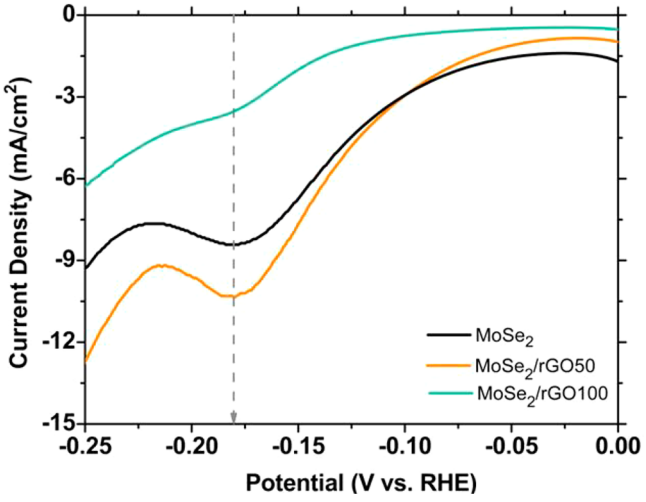

Figure 5. Polarization curves of the as-synthesized $MoSe_2$, $MoSe_2$/rGO50, and $MoSe_2$/rGO100 during their first scan generated in 0.5 M H_2SO_4 at 5 mV/s.

during the microwave process.[47,48] The above peak of GO was not noticed in the as-synthesized and the annealed hybrids indicating reduction of GO to rGO. The XRD peak of rGO was not clearly distinguished in the presence of $MoSe_2$.[44] The XRD pattern of $MoSe_2$/rGO100 demonstrated partial crystallinity of $MoSe_2$, which could be due to the shorter reaction period and relatively low temperature under the microwave process. As a result of annealing, $MoSe_2$ became crystalline and distinct indexed peaks indicated the formation of hexagonal $MoSe_2$ (JCPDS card no. 87-2419).[34,49] Corresponding XRD patterns of $MoSe_2$/rGO50 and its annealed counterpart are presented in Figure S2a, whereas Figure S2b shows the XRD patterns of $MoSe_2$ and $MoSe_2$_400 °C. Similar transformation from a partial crystalline phase to 2H crystalline phase of $MoSe_2$ was observed in both Figure S2a and Figure S2b. Figure 2b shows the TEM image of thin layered GO prepared by the modified Hummers method.[44] TEM images of $MoSe_2$/rGO100 (Figure 2c and Figure S3a) reveal that microwave process resulted in the growth of probable amorphous and few layers of disorderly distributed partially crystalline $MoSe_2$ on rGO. Annealing of $MoSe_2$/rGO100 induced crystallinity, and $MoSe_2$ layers were found significantly organized on rGO without noticeable agglomeration as shown in Figure 2d and Figure S3b. An interlayer spacing of ∼0.65 nm corresponds to (002) plane of hexagonal $MoSe_2$ in $MoSe_2$/rGO100_400 °C. TEM images of $MoSe_2$/rGO50 and $MoSe_2$/rGO50_400 °C are presented in Figures S3c and S3d, respectively, and they demonstrate reduced agglomeration as well although $MoSe_2$ content with rGO was expected to be higher. However, in the absence ofGO, a relatively larger size distribution of as-synthesized $MoSe_2$ was observed (Figure S3e). Moreover, annealing of plain $MoSe_2$ was likely to cause agglomeration, and a relevant image is presented in Figure S3f. As a result, introduction of GO not only is beneficial in controlling the growth of $MoSe_2$ but also significantly prevents the agglomeration of $MoSe_2$ layers during annealing. Such morphological changes of $MoSe_2$ associated with/without rGO in both as-synthesized and annealed samples are expected to demonstrate varied electrocatalytic activities.

Structural properties were further investigated using the Raman spectroscopy. Representative Raman spectra of $MoSe_2$/rGO100 and $MoSe_2$/rGO100_400 °C are presented in Figure 3. A wide asymmetric peak was detected at 252.88 cm^{-1}, indicating the Se−Se stretching vibration mode of weakly packed polymer chains of amorphous Se (a-Se).[16,29,50,51] A shoulder at ∼235.34 cm^{-1} with low intensity may correspond to thermodynamically stable trigonal Se[50,51] and/or A_{1g} Raman mode (out-of-plane vibration of Se atoms) of partially crystalline $MoSe_2$,[52] whereas another relatively high energy shoulder at 263.82 cm^{-1} was assigned to the intra-ring bond stretching vibration of Se_8.[50,51] E^1_{2g} mode (in-plane vibration of Mo and Se atoms) of $MoSe_2$ was not clearly visible in the Raman spectrum of $MoSe_2$/rGO100. However, marked changes were observed in the Raman spectrum of $MoSe_2$/rGO100_400 °C. The obvious vibrational band of loosely packed polymer chains of Se was absent. Rather, $MoSe_2$ in the annealed hybrid exhibited distinct A_{1g} (at 238.83 cm^{-1}) and E^1_{2g} (at 286.50 cm^{-1}) Raman-active modes.[9,53] Although the A_{1g} mode of $MoSe_2$ in the annealed hybrid was red-shifted in comparison to the reported value of bulk $MoSe_2$,[54] its blue-shift

DOI: 10.1021/acsanm.8b00208
ACS Appl. Nano Mater. 2018, 1, 2143−2152

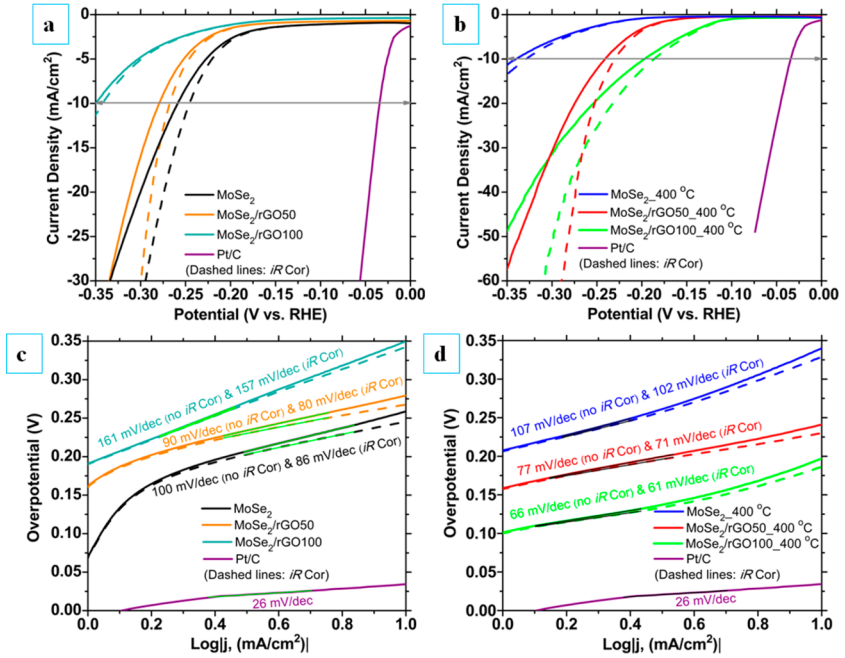

Figure 6. Polarization curves of (a) the as-synthesized and (b) annealed catalysts generated in 0.5 M H_2SO_4 at 5 mV/s. Corresponding Tafel plots of the as-synthesized and annealed samples presented in (c) and (d), respectively. *iR* corrected outcomes represented by dashed lines.

Table 1. Overall HER Properties of the As-Synthesized and Their Corresponding Annealed Counterparts Measured in 0.5 M H_2SO_4

	iR corrected results		
electrocatalyst	overpotential (mV) at j = 10 mA/cm^2	Tafel slope (mV/dec)	charge transfer resistance (Ω)
$MoSe_2$	246	86	115
$MoSe_2$_400 °C	328	102	1914
$MoSe_2$/rGO50	268	80	166
$MoSe_2$/rGO50_400 °C	230	71	68
$MoSe_2$/rGO100	342	157	788
$MoSe_2$/rGO100_400 °C	186	61	25

with respect to that of $MoSe_2$/rGO100 suggested a relative increase of interlayer interaction due to improved crystallinity.[52,55] On the other hand, the approximate intensity ratio of A_{1g} to E^1_{2g} is ∼10:1, comparable to that of an edge-terminated $MoSe_2$ grown on Si nanowire (13:1).[56] It suggests that $MoSe_2$ in $MoSe_2$/rGO100_400 °C retained significantly high number of active sites although annealing might reduce the catalytic edge sites to some extent.[57] Therefore, it could be conferred that rGO in the hybrid noticeably restricted agglomeration of $MoSe_2$. Moreover, rGO in both $MoSe_2$/rGO100 and $MoSe_2$/rGO100_400 °C demonstrated the D and G bands at ∼1335 and ∼1596 cm^{-1}, respectively. The G band arises from the vibration of the sp^2-hybridized carbon, and the D band is associated with structural imperfection and defects. The I_D/I_G value of the annealed hybrid (1.23) was found to be greater than that of $MoSe_2$/rGO100 (1.08), signifying the presence of higher degree of structural defects in $MoSe_2$/rGO100_400 °C.[30,58]

XPS analyses were conducted to investigate the composition and elemental valence states in $MoSe_2$ with its rGO hydrids. Survey spectra of $MoSe_2$/rGO100, $MoSe_2$/rGO100_400 °C, $MoSe_2$/rGO50, and $MoSe_2$/rGO50_400 °C are shown in Figure S4a–d, suggesting the coexistence Mo, Se, C, and O. Deconvoluted XPS spectra of Mo, Se, and C of $MoSe_2$/rGO100 and $MoSe_2$/rGO100_400 °C are presented in Figure 4a–f. Two peaks located at 229 eV (Mo $3d_{5/2}$) and 232.10 eV

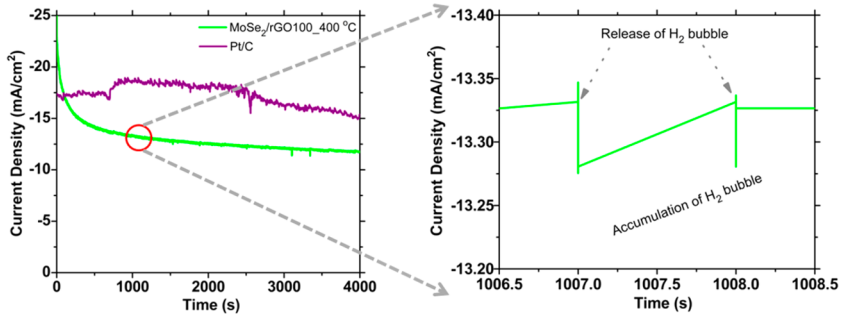

Figure 7. Stability (j–t) test of $MoSe_2$/rGO100_400 °C at η = 245 mV and Pt/C at η = 42 mV with an enlarged view of $MoSe_2$/rGO100_400 °C demonstrating continuous hydrogen bubble accumulation and release in 0.5 M H_2SO_4.

DOI: 10.1021/acsanm.8b00208
ACS Appl. Nano Mater. 2018, 1, 2143–2152

($Mo\ 3d_{3/2}$) in Figure 4a confirmed Mo^{4+} state of molybdenum in the as-synthesized hybrid. In general, $Mo\ 3d_{5/2}$ of Mo^{6+} state in molybdates, MoO_3, and $MoSe_{x\geq 3}$ are observed from 232 to 233.30 eV.[16,59−61] The doublet for $Mo\ 3d_{5/2}$ (at 232.50 eV) and $Mo\ 3d_{3/2}$ (at 235.80 eV) were related to the Mo^{6+} state. On the other hand, Figure 4b shows a relative increase in intensities for Mo^{4+} and a decrease for Mo^{6+} in $MoSe_2$/rGO100_400 °C. Mo^{6+} and Mo^{4+} state demonstrated similar changes in $MoSe_2$/rGO50 (Figure S5a) and $MoSe_2$/rGO50_400 °C (Figure S5b). The Se 3d peak of Se^0 is usually observed between 54.9 and 56.3 eV, whereas it is detected at a relatively lower binding energy in the case of Se^{2-}.[16,62,63] The doublet at 54.50 and 55.2 eV corresponding to $Se\ 3d_{5/2}$ and $Se\ 3d_{3/2}$ (Figure 4c), respectively, confirmed the presence of Se^{2-}. The other doublet at higher energies indicated Se^0. The deconvoluted peaks of Se in $MoSe_2$/rGO100_400 °C (Figure 4d) demonstrated an increase in the intensities for Se^{2-} and a reduction for Se^0, which were comparable to the observations of oxidation states of Mo in Figure 4b. The conversion of Mo^{6+} in the presence of excess Se^0 into $MoSe_2$ could have occurred, and some selenium evaporated due to the elevated temperature annealing. The Mo:Se ratio changed from 4.34 to 2.36 as a result of annealing of $MoSe_2$/rGO100. An analogous modification was also observed from a relative broadening of the Se 3d spectrum in $MoSe_2$/rGO50 (Figure S5c) to its shift to the lower binding energy in $MoSe_2$/rGO50_400 °C (Figure S5d). XPS analysis of the C 1s peak in $MoSe_2$/rGO100 showed that hydrazine assisted microwave process was beneficial to convert GO into rGO (Figure 4e).[64] However, rGO was further reduced as a result of annealing indicated by the smaller intensities of oxygenated functional groups as shown in Figure 4f. The C 1s spectrum of $MoSe_2$/rGO50 was also found to change accordingly as a result of annealing (Figure S5e,f). The minor C−N peak ~285.95 eV in the annealed hybrids of $MoSe_2$ with rGO could be due to the presence of decomposed products of hydrazine that might have existed within the as-synthesized samples (Figure S6a−d).[65,66]

Moreover, FTIR spectroscopic analyses of GO, $MoSe_2$/rGO100, and $MoSe_2$/rGO100_400 °C as shown in Figure S7 confirmed the formation of GO and supported the observations of an incremental reduction of oxygenated functional groups by the microwave process and the subsequent annealing under argon gas flow. Therefore, an improvement in the electrocatalytic performance can be expected for the annealed hybrids of $MoSe_2$ with rGO.

Electrochemical Performance of the Catalysts. The HER activities were investigated with 0.5 M H_2SO_4 under a three-electrode cell. A desired HER catalyst should exhibit a high current density at a low overpotential.[12,9] As part of electrocatalytic evaluation, polarization curves obtained during the first scan for the as-synthesized samples are presented in Figure 5. A reduction peak was observed at about −183 mV vs RHE, and current density subsequently increased due to hydrogen evolution at further negative potentials. This particular cathodic peak was associated with the formation of H_2Se in the acidic media via the reaction: $Se^0 + 2H^+ + 2e^- = H_2Se$.[67−70] Unreacted amorphous Se was likely to transform to H_2Se during the first cathodic scan at lower overpotential as observed in Raman (Figure 3) and the XPS spectra (Figure 4c and Figure S5c). Therefore, the cathodic current density during the first polarization involved the generation of both H_2Se and H_2 gases. Catalytic properties of as-synthesized samples can only be realized, when polarization curves reflect solely electrocatalytic hydrogen generation. Interestingly, the cathodic peak associated with H_2Se formation was not detected in the subsequent scans, indicating an irreversible conversion of the deposited as-synthesized film into an actual HER catalyst during the first polarization, and a similar observation was also addressed for electrodeposited amorphous MoS_x.[28,71,72] Therefore, the second polarization curve as shown in Figure 6a was considered to examine the HER activity of the as-synthesized catalysts. However, such a reductive peak was not observed during the LSV polarization of the corresponding annealed catalysts, and the respective polarization curves are presented in Figure 6b.

One of the criteria of interest in order to examine the HER activity of the electrocatalysts is the onset potential defined as the potential, where first electrocatalytic hydrogen evolution occurs.[12,34] As-synthesized $MoSe_2$ and its rGO hybrids exhibited a low onset potential with a value of about −44 mV vs RHE (Figure S8a). On the other hand, their annealed counterparts demonstrated a dramatic change in the onset potential as presented in Figure S8b. $MoSe_2$/rGO100_400 °C showed its onset potential at −46 mV vs RHE, which was close to that of $MoSe_2$/rGO100. With the reduction of GO content, the elevated temperature annealing drove further negative shift in the onset potential of $MoSe_2$/rGO50_400 °C (−79 mV vs RHE) and $MoSe_2$_400 °C (−130 mV vs RHE). Therefore, it can be inferred that changes associated with the onset potential were due to both the active sites and the conductive nature of rGO. Plain rGO demonstrates negligible HER activity.[73] Realistic assessment of the electrocatalytic process is often performed with a correction associated with the Ohmic loss throughout the system. Therefore, *iR* corrected polarization curves are also presented in Figure 6a,b. A comparative analysis on the requirement of overpotential to produce a cathodic current density of 10 mA/cm^2 (Figure 6a,b and Figure S9a−c) revealed the benefit of annealing of $MoSe_2$ with rGO, whereas it was counterproductive for as-synthesized $MoSe_2$. $MoSe_2$/rGO100_400 °C displayed a remarkably improved overpotential of 195 mV for −10 mA/cm^2, which was 154 mV less than that of $MoSe_2$/rGO100. As a result of *iR* correction, overpotential requirement is reduced to 186 mV for $MoSe_2$/rGO100_400 °C. Similarly, $MoSe_2$/rGO50_400 °C with an overpotential of 230 mV (241 mV for without *iR* correction) exhibited its superior catalytic activity over $MoSe_2$/rGO50. On the contrary, the as-synthesized $MoSe_2$ showed a smaller requirement of overpotential requirement at −10 mA/cm^2 in comparison to that of $MoSe_2$_400 °C. Kong et al. demonstrated for the edge-terminated MoS_2 that the elevated temperature annealing led to the reduction of the number of active sites and consequently reduced HER activity, although crystallinity was improved.[57] It essentially affirmed that the number of active sites in plain $MoSe_2$ dominated over the crystallinity for the improvement of the HER performance. Therefore, the incorporation of $MoSe_2$ with highly conductive rGO could be beneficial to enhance the HER activities, which were apparent from TEM image, Raman, and XPS analyses described earlier. Since active sites are mostly located at the edge planes and defects, such improved electrocatalytic activities of the annealed hybrids of $MoSe_2$ and rGO could be credited to the presence of numerous active sites within the few layered $MoSe_2$ and a facilitated charge transport process as a result of the direct contact between the catalyst and the highly conductive rGO. Furthermore, the intersection point at about −32 mA/cm^2 (with/without *iR* correction) in Figure 6b

DOI: 10.1021/acsanm.8b00208
ACS Appl. Nano Mater. 2018, 1, 2143−2152

suggested that $MoSe_2$/rGO100_400 °C should serve better for the devices with a low cathodic current density (<|−32 mA/cm^2|); whereas, $MoSe_2$/rGO50_400 °C would be beneficial for the high cathodic current density (>|−32 mA/cm^2|) devices.[12] Such alteration in the polarization curves was likely to be associated with the mass transport.[74]

Tafel plots were generated to examine the reaction pathway of hydrogen evolution for the catalysts. Tafel plots of the as-synthesized samples and their corresponding annealed counterparts are presented in Figures 6c and 6d, respectively. Generally, the linear region of a Tafel plot is fit with the Tafel equation $\eta = b \log|j| + a$; η, b, and j are overpotential, Tafel slope, and current density, respectively. Lower value in the Tafel slope is desired, and its value implies the additional voltage required to boost the current density by an order of magnitude.[12] Three possible reaction mechanisms for the hydrogen evolution reaction in an acidic media have been proposed:[32,75]

(A) Volmer reaction: $H_3O^+ + e^- \rightarrow H_{ads} + H_2O$ [discharge step]; $b = \frac{2.3RT}{\alpha F} \approx 120$ mV

B. Heyrovsky reaction: $H_3O^+ + H_{ads} + e^- \rightarrow H_2 + H_2O$ [electrochemical desorption step]; $b = \frac{2.3RT}{(1+\alpha)F} \approx 40$ mV

(C) Tafel reaction: $2H_{ads} \rightarrow H_2$ [recombination step]; $b = \frac{2.3RT}{2F} \approx 30$ mV; b = Tafel slope, T = absolute temperature, R = molar gas constant, F = Faraday constant, and α = symmetry coefficient (~0.5).

The HER activities follow either Volmer−Tafel or Volmer−Heyrovsky reaction pathway. Pt/C with a small Tafel slope of 26 mV/dec was expected to follow the Volmer−Tafel mechanism, where the Tafel reaction was the rate-limiting step at low overpotential.[32] Relatively higher Tafel slopes for the as-synthesized catalysts, i.e., $MoSe_2$(86 mV/dec), $MoSe_2$/rGO50 (80 mV/dec), and $MoSe_2$/rGO100 (157 mV/dec), were indicative of slower electron transport.[74] In the absence of *iR* correction, the respective Tafel slopes were relatively greater. However, $MoSe_2$/rGO100_400 °C, in particular, demonstrated an outstandingly smaller Tafel slope of 61 mV/dec (66 mV/dec for without *iR* correction) in comparison to that of $MoSe_2$/rGO100, and hydrogen evolution might proceed via the Volmer−Heyrovsky pathway.[76] $MoSe_2$/rGO50_400 °C similarly demonstrated a smaller Tafel slope of 71 mV/dec (77 mV/dec for without *iR* correction). On the contrary, annealing and absence of rGO led to an inferior performance of $MoSe_2$_400 °C in comparison to as-synthesized $MoSe_2$. It is noteworthy that the appropriate analysis of the Tafel slope is still incomplete because of the complexities of various reaction steps involving the HER.[75,77] Above all, $MoSe_2$/rGO100_400 °C demonstrated promising HER properties in comparison to other reported electrocatalysts as shown in Table S1.

Electrochemical impedance spectroscopic (EIS) measurements were performed to determine charge-transfer resistance (R_{ct}) during the hydrogen evolution reaction. R_{ct} largely corresponds to the HER kinetics at the electrode−electrolyte interface at low frequencies.[78,79] The Nyquist plots of the as-synthesized and the annealed samples are presented in Figures S10a and S10b, respectively. The plots exhibited two semicircles and were fit with a two-time constant model, and the equivalent circuit diagram is depicted in Figure S10c. Although R_{ct} was found to increase with the incremental rGO content for the as-synthesized samples, a dramatic transformation in the EIS performance was observed for the annealed catalysts. R_{ct} value in $MoSe_2$/rGO100 changed from ~788 to 25 Ω in $MoSe_2$/rGO100_400 °C, indicating faster electron transfer process due to annealing. $MoSe_2$/rGO50_400 °C similarly demonstrated a reduced R_{ct} value of 68 Ω in comparison to that of $MoSe_2$/rGO50 (166 Ω). On the contrary, annealing was found to be detrimental for as-synthesized $MoSe_2$ as revealed with the higher value of R_{ct}. The values of the series resistance (R_s), the charge transfer resistance (R_{ct}), and the HER current density observed at an applied overpotential of 205 mV are shown in Table S2. The relationship between the HER current density and the R_{ct} values underscores that the synergistic effect between highly conductive rGO and exposed sites of $MoSe_2$ in the hybrids resulted in enhanced HER performance for both $MoSe_2$/rGO50_400 °C and $MoSe_2$/rGO100_400 °C. Highlights of the HER activities are presented in the Table 1. Moreover, the stability test for the as-synthesized $MoSe_2$, $MoSe_2$/rGO100_400 °C, and Pt/C was carried out using the chronoamperometric method (j−t) at an overpotential of 245 mV, and the corresponding j−t plot for continuous hydrogen generation is shown in Figure 7. In comparison to Pt/C, current density of $MoSe_2$/rGO100_400 °C remained fairly stable over 4000 s, which suggests that it was a viable HER catalyst. The decay in the current density was likely due to the blockage of the catalytic active sites by the accumulated hydrogen bubble and the loss of some active sites associated with the rotational electrode. An enlarged view of the stability plot showed the alternate process of hydrogen bubble accumulation and its release. The region between two consecutive bubble releases emphasized the accumulation of the molecular hydrogen on the electrode surface. A stability plot generated at the same overpotential for as-synthesized $MoSe_2$ is presented in Figure S11.

CONCLUSION

In summary, we have demonstrated the synthesis of $MoSe_2$ and its few layered hybrids with rGO using a simple one-pot microwave process followed by annealing under an inert gas flow. Annealing introduced crystallinity in $MoSe_2$ from its partially crystalline form and improved the conductivity of its rGO hybrids. The electrocatalytic activities revealed that the as-synthesized samples required catalytic activation prior to the evaluation of the HER performance. Although annealing of partially crystalline $MoSe_2$ adversely impacted the catalytic activity, the annealed hybrids of $MoSe_2$ with rGO outperformed their as-synthesized counterparts and $MoSe_2$. The enhanced HER activity is due to the synergistic effect between highly conductive rGO and catalytically active $MoSe_2$. Apart from good stability, the best electrocatalytic performance demonstrated by the hybrid was an overpotential of 186 mV at −10 mA/cm^2 and a smaller Tafel slope of 61 mV/dec Therefore, this study would be beneficial to develop and realize the potential of other noble metal-free electrode materials applicable to the energy storage and conversion.

ASSOCIATED CONTENT

Supporting Information

The Supporting Information is available free of charge on the ACS Publications website at DOI: 10.1021/acsanm.8b00208.

Reference electrode calibration, XRD patterns of $MoSe_2$/rGO50 and $MoSe_2$/rGO50_400 °C and $MoSe_2$ and $MoSe_2$_400 °C; representative TEM images of $MoSe_2$/

DOI: 10.1021/acsanm.8b00208
ACS Appl. Nano Mater. 2018, 1, 2143−2152

rGO100, $MoSe_2$/rGO100_400 °C, $MoSe_2$/rGO50, $MoSe_2$/rGO50_400 °C, $MoSe_2$, and $MoSe_2$_400 °C; survey XPS spectra of $MoSe_2$/rGO100, $MoSe_2$/rGO100_400 °C, $MoSe_2$/rGO50, and $MoSe_2$/rGO50_400 °C; XPS spectra of Mo 3d, Se 3d, and C 1s of in $MoSe_2$/rGO50, and $MoSe_2$/rGO50_400 °C; N 1s XPS spectra of $MoSe_2$/rGO100, $MoSe_2$/rGO100_400 °C, $MoSe_2$/rGO50, and $MoSe_2$/rGO50_400 °C; FTIR spectra of graphene oxide, $MoSe_2$/rGO100, and $MoSe_2$/rGO100_400 °C; determination of the onset potential of as-synthesized samples after catalytic activation using linear sweep voltammetry and annealed samples; change in the electrocatalytic HER activity as a result of annealing of the as-synthesized samples $MoSe_2$ vs $MoSe_2$_400 °C, $MoSe_2$/rGO50 vs $MoSe_2$/rGO50_400 °C, and $MoSe_2$/rGO100 vs $MoSe_2$/rGO100_400 °C; table of comparative HER performance among different catalysts; Nyquist plots of the as-synthesized and the annealed samples and corresponding equivalent simulated circuit diagram; table for series resistance, charge transfer resistance, and corresponding current density; *j*–*t* plot for the as-synthesized $MoSe_2$ (PDF)

AUTHOR INFORMATION

Corresponding Author

*(H.L.) E-mail hluo@nmsu.edu.

ORCID

Sanjib Das: 0000-0002-5281-4458

Hongmei Luo: 0000-0002-9546-761X

Present Address

J.P.: National Nuclear Laboratory (Workington Laboratory), Havelock Rd, Derwent Howe, Workington, CA143YQ, UK.

Author Contributions

All authors have given approval to the final version of the manuscript. Sarker, Peters, and Richins conducted the materials synthesis; Chen and Das performed XPS; Li helped with HRTEM; Chen run the Raman spectra; Yan and Zhou helped with the electrochemical analysis. Luo managed the project. All authors contributed to the paper writing.

Notes

The authors declare no competing financial interest.

ACKNOWLEDGMENTS

H. Luo acknowledges the funding support from New Mexico EPSCoR with NSF-1301346. B. Li thanks the China Dongguan foundation #2015508102006. This work made use of the Keck-II facility of Northwestern University's NUANCE Center, which has received support from the Soft and Hybrid Nanotechnology Experimental (SHyNE) Resource (NSF ECCS-1542205); the MRSEC program (NSF DMR-1121262) at the Materials Research Center; the International Institute for Nanotechnology (IIN); the Keck Foundation; and the State of Illinois, through the IIN.

REFERENCES

(1) Turner, J. A. Sustainable Hydrogen Production. *Science* **2004**, *305* (5686), 972–974.

(2) Wan, C.; Regmi, Y. N.; Leonard, B. M. Multiple Phases of Molybdenum Carbide as Electrocatalysts for the Hydrogen Evolution Reaction. *Angew. Chem.* **2014**, *126* (25), 6525–6528.

(3) Xiang, Q.; Yu, J.; Jaroniec, M. Synergetic Effect of MoS_2 and Graphene as Cocatalysts for Enhanced Photocatalytic H_2 Production Activity of TiO_2 Nanoparticles. *J. Am. Chem. Soc.* **2012**, *134* (15), 6575–6578.

(4) Tian, Y.; Ge, L.; Wang, K.; Chai, Y. Synthesis of Novel MoS_2/g-C_3N_4 Heterojunction Photocatalysts with Enhanced Hydrogen Evolution Activity. *Mater. Charact.* **2014**, *87*, 70–73.

(5) Hou, Y.; Abrams, B. L.; Vesborg, P. C. K.; Björketun, M. E.; Herbst, K.; Bech, L.; Setti, A. M.; Damsgaard, C. D.; Pedersen, T.; Hansen, O.; Rossmeisl, J.; Dahl, S.; Nørskov, J. K.; Chorkendorff, I. Bioinspired Molecular Co-Catalysts Bonded to a Silicon Photocathode for Solar Hydrogen Evolution. *Nat. Mater.* **2011**, *10*, 434–438.

(6) Lu, Q.; Yu, Y.; Ma, Q.; Chen, B.; Zhang, H. 2D Transition-Metal-Dichalcogenide-Nanosheet-Based Composites for Photocatalytic and Electrocatalytic Hydrogen Evolution Reactions. *Adv. Mater.* **2016**, *28* (10), 1917–1933.

(7) Zhang, J.; Cui, R.; Li, X.; Liu, X.; Huang, W. A Nanohybrid Consisting of $NiPS_3$ Nanoparticles Coupled with Defective Graphene as a pH-Universal Electrocatalyst for Efficient Hydrogen Evolution. *J. Mater. Chem. A* **2017**, *5* (45), 23536–23542.

(8) Zhou, W.; Jia, J.; Lu, J.; Yang, L.; Hou, D.; Li, G.; Chen, S. Recent Developments of Carbon-Based Electrocatalysts for Hydrogen Evolution Reaction. *Nano Energy* **2016**, *28*, 29–43.

(9) Tang, H.; Dou, K.; Kaun, C.-C.; Kuang, Q.; Yang, S. $MoSe_2$ Nanosheets and Their Graphene Hybrids: Synthesis, Characterization and Hydrogen Evolution Reaction Studies. *J. Mater. Chem. A* **2014**, *2* (2), 360–364.

(10) Wu, W.; Tang, Z.; Wang, K.; Liu, Z.; Li, L.; Chen, S. Peptide Templated AuPt Alloyed Nanoparticles as Highly Efficient Bi-Functional Electrocatalysts for Both Oxygen Reduction Reaction and Hydrogen Evolution Reaction. *Electrochim. Acta* **2018**, *260*, 168–176.

(11) Peng, Y.; Pan, W.; Wang, N.; Lu, J.; Chen, S. Ruthenium Ion-Complexed Graphitic Carbon Nitride Nanosheets Supported on Reduced Graphene Oxide as High-Performance Catalysts for Electrochemical Hydrogen Evolution. *ChemSusChem* **2018**, *11* (1), 130–136.

(12) Benck, J. D.; Hellstern, T. R.; Kibsgaard, J.; Chakthranont, P.; Jaramillo, T. F. Catalyzing the Hydrogen Evolution Reaction (HER) with Molybdenum Sulfide Nanomaterials. *ACS Catal.* **2014**, *4* (11), 3957–3971.

(13) Yan, Y.; Xia, B.; Xu, Z.; Wang, X. Recent Development of Molybdenum Sulfides as Advanced Electrocatalysts for Hydrogen Evolution Reaction. *ACS Catal.* **2014**, *4* (6), 1693–1705.

(14) McKone, J. R.; Sadtler, B. F.; Werlang, C. A.; Lewis, N. S.; Gray, H. B. Ni–Mo Nanopowders for Efficient Electrochemical Hydrogen Evolution. *ACS Catal.* **2013**, *3* (2), 166–169.

(15) Lukowski, M. A.; Daniel, A. S.; Meng, F.; Forticaux, A.; Li, L.; Jin, S. Enhanced Hydrogen Evolution Catalysis from Chemically Exfoliated Metallic MoS_2 Nanosheets. *J. Am. Chem. Soc.* **2013**, *135* (28), 10274–10277.

(16) Saadi, F. H.; Carim, A. I.; Velazquez, J. M.; Baricuatro, J. H.; McCrory, C. C. L.; Soriaga, M. P.; Lewis, N. S. Operando Synthesis of Macroporous Molybdenum Diselenide Films for Electrocatalysis of the Hydrogen-Evolution Reaction. *ACS Catal.* **2014**, *4* (9), 2866–2873.

(17) Huang, Z.; Chen, Z.; Chen, Z.; Lv, C.; Humphrey, M. G.; Zhang, C. Cobalt Phosphide Nanorods as an Efficient Electrocatalyst for the Hydrogen Evolution Reaction. *Nano Energy* **2014**, *9*, 373–382.

(18) Ge, C.; Jiang, P.; Cui, W.; Pu, Z.; Xing, Z.; Asiri, A. M.; Obaid, A. Y.; Sun, X.; Tian, J. Shape-Controllable Synthesis of Mo_2C Nanostructures as Hydrogen Evolution Reaction Electrocatalysts with High Activity. *Electrochim. Acta* **2014**, *134*, 182–186.

(19) Jia, J.; Xiong, T.; Zhao, L.; Wang, F.; Liu, H.; Hu, R.; Zhou, J.; Zhou, W.; Chen, S. Ultrathin N-Doped Mo_2C Nanosheets with Exposed Active Sites as Efficient Electrocatalyst for Hydrogen Evolution Reactions. *ACS Nano* **2017**, *11* (12), 12509–12518.

(20) Tsai, C.; Chan, K.; Abild-Pedersen, F.; Norskov, J. K. Active Edge Sites in $MoSe_2$ and WSe2 Catalysts for the Hydrogen Evolution Reaction: A Density Functional Study. *Phys. Chem. Chem. Phys.* **2014**, *16* (26), 13156–13164.

(21) Liu, N.; Yang, L.; Wang, S.; Zhong, Z.; He, S.; Yang, X.; Gao, Q.; Tang, Y. Ultrathin MoS_2 Nanosheets Growing within an in-Situ-

DOI: 10.1021/acsanm.8b00208
ACS Appl. Nano Mater. 2018, 1, 2143–2152

Formed Template as Efficient Electrocatalysts for Hydrogen Evolution. *J. Power Sources* **2015**, *275*, 588−594.
(22) Xu, M.; Liang, T.; Shi, M.; Chen, H. Graphene-Like Two-Dimensional Materials. *Chem. Rev.* **2013**, *113* (5), 3766−3798.
(23) Yan, H.; Tian, C.; Wang, L.; Wu, A.; Meng, M.; Zhao, L.; Fu, H. Phosphorus-Modified Tungsten Nitride/Reduced Graphene Oxide as a High-Performance, Non-Noble-Metal Electrocatalyst for the Hydrogen Evolution Reaction. *Angew. Chem., Int. Ed.* **2015**, *54* (21), 6325−6329.
(24) Chen, X.; Wang, Z.; Qiu, Y.; Zhang, J.; Liu, G.; Zheng, W.; Feng, W.; Cao, W.; Hu, P.; Hu, W. Controlled Growth of Vertical 3D $MoS_{2(1-x)}Se_{2x}$ Nanosheets for an Efficient and Stable Hydrogen Evolution Reaction. *J. Mater. Chem. A* **2016**, *4* (46), 18060−18066.
(25) Laursen, A. B.; Kegnaes, S.; Dahl, S.; Chorkendorff, I. Molybdenum Sulfides-Efficient and Viable Materials for Electro - and Photoelectrocatalytic Hydrogen Evolution. *Energy Environ. Sci.* **2012**, *5* (2), 5577−5591.
(26) Qu, B.; Yu, X.; Chen, Y.; Zhu, C.; Li, C.; Yin, Z.; Zhang, X. Ultrathin MoSe2 Nanosheets Decorated on Carbon Fiber Cloth as Binder-Free and High-Performance Electrocatalyst for Hydrogen Evolution. *ACS Appl. Mater. Interfaces* **2015**, *7* (26), 14170−14175.
(27) Voiry, D.; Fullon, R.; Yang, J.; de Carvalho Castro e Silva, C.; Kappera, R.; Bozkurt, I.; Kaplan, D.; Lagos, M. J.; Batson, P. E.; Gupta, G.; Mohite, A. D.; Dong, L.; Er, D.; Shenoy, V. B.; Asefa, T.; Chhowalla, M. The Role of Electronic Coupling between Substrate and 2D MoS_2 Nanosheets in Electrocatalytic Production of Hydrogen. *Nat. Mater.* **2016**, *15*, 1003−1009.
(28) Ting, L. R. L.; Deng, Y.; Ma, L.; Zhang, Y.-J.; Peterson, A. A.; Yeo, B. S. Catalytic Activities of Sulfur Atoms in Amorphous Molybdenum Sulfide for the Electrochemical Hydrogen Evolution Reaction. *ACS Catal.* **2016**, *6* (2), 861−867.
(29) Redman, D. W.; Rose, M. J.; Stevenson, K. J. Electrodeposition of Amorphous Molybdenum Chalcogenides from Ionic Liquids and Their Activity for the Hydrogen Evolution Reaction. *Langmuir* **2017**, *33* (37), 9354−9360.
(30) Mao, S.; Wen, Z.; Ci, S.; Guo, X.; Ostrikov, K.; Chen, J. Perpendicularly Oriented $MoSe_2$/Graphene Nanosheets as Advanced Electrocatalysts for Hydrogen Evolution. *Small* **2015**, *11* (4), 414−419.
(31) Xu, C.; Peng, S.; Tan, C.; Ang, H.; Tan, H.; Zhang, H.; Yan, Q. Ultrathin S-Doped $MoSe_2$ Nanosheets for Efficient Hydrogen Evolution. *J. Mater. Chem. A* **2014**, *2* (16), 5597−5601.
(32) Li, Y.; Wang, H.; Xie, L.; Liang, Y.; Hong, G.; Dai, H. MoS_2 Nanoparticles Grown on Graphene: An Advanced Catalyst for the Hydrogen Evolution Reaction. *J. Am. Chem. Soc.* **2011**, *133* (19), 7296−7299.
(33) Zhang, L.; Sun, L.; Huang, Y.; Sun, Y.; Hu, T.; Xu, K.; Ma, F. Hydrothermal Synthesis of N-Doped RGO/$MoSe_2$ Composites and Enhanced Electro-Catalytic Hydrogen Evolution. *J. Mater. Sci.* **2017**, *52* (23), 13561−13571.
(34) Huang, Y.; Lu, H.; Gu, H.; Fu, J.; Mo, S.; Wei, C.; Miao, Y.-E.; Liu, T. A CNT@$MoSe_2$ Hybrid Catalyst for Efficient and Stable Hydrogen Evolution. *Nanoscale* **2015**, *7* (44), 18595−18602.
(35) Cui, W.; Ge, C.; Xing, Z.; Asiri, A. M.; Sun, X. Ni_xS_y-MoS_2 Hybrid Microspheres: One-Pot Hydrothermal Synthesis and Their Application as a Novel Hydrogen Evolution Reaction Electrocatalyst with Enhanced Activity. *Electrochim. Acta* **2014**, *137*, 504−510.
(36) Zhang, J.; Wang, Q.; Wang, L.; Li, X.; Huang, W. Layer-Controllable WS_2-Reduced Graphene Oxide Hybrid Nanosheets with High Electrocatalytic Activity for Hydrogen Evolution. *Nanoscale* **2015**, *7* (23), 10391−10397.
(37) Guo, J.; Li, F.; Sun, Y.; Zhang, X.; Tang, L. Oxygen-Incorporated MoS_2 Ultrathin Nanosheets Grown on Graphene for Efficient Electrochemical Hydrogen Evolution. *J. Power Sources* **2015**, *291*, 195−200.
(38) Youn, D. H.; Han, S.; Kim, J. Y.; Kim, J. Y.; Park, H.; Choi, S. H.; Lee, J. S. Highly Active and Stable Hydrogen Evolution Electrocatalysts Based on Molybdenum Compounds on Carbon Nanotube−Graphene Hybrid Support. *ACS Nano* **2014**, *8* (5), 5164−5173.
(39) Lai, F.; Yong, D.; Ning, X.; Pan, B.; Miao, Y.-E.; Liu, T. Carbon Nanofibers: Bionanofiber Assisted Decoration of Few-Layered $MoSe_2$ Nanosheets on 3D Conductive Networks for Efficient Hydrogen Evolution. *Small* **2017**, *13* (7), 1602866.
(40) Zhang, Y.; Zuo, L.; Zhang, L.; Huang, Y.; Lu, H.; Fan, W.; Liu, T. Cotton Wool Derived Carbon Fiber Aerogel Supported Few-Layered $MoSe_2$ Nanosheets As Efficient Electrocatalysts for Hydrogen Evolution. *ACS Appl. Mater. Interfaces* **2016**, *8* (11), 7077−7085.
(41) Li, Y.; Yu, Y.; Huang, Y.; Nielsen, R. A.; Goddard, W. A.; Li, Y.; Cao, L. Engineering the Composition and Crystallinity of Molybdenum Sulfide for High-Performance Electrocatalytic Hydrogen Evolution. *ACS Catal.* **2015**, *5* (1), 448−455.
(42) Ekspong, J.; Sharifi, T.; Shchukarev, A.; Klechikov, A.; Wågberg, T.; Gracia-Espino, E. Stabilizing Active Edge Sites in Semicrystalline Molybdenum Sulfide by Anchorage on Nitrogen-Doped Carbon Nanotubes for Hydrogen Evolution Reaction. *Adv. Funct. Mater.* **2016**, *26* (37), 6766−6776.
(43) Gong, Q.; Cheng, L.; Liu, C.; Zhang, M.; Feng, Q.; Ye, H.; Zeng, M.; Xie, L.; Liu, Z.; Li, Y. Ultrathin $MoS_{2(1-x)}Se_{2x}$ Alloy Nanoflakes For Electrocatalytic Hydrogen Evolution Reaction. *ACS Catal.* **2015**, *5* (4), 2213−2219.
(44) Yan, L.; Chen, G.; Sarker, S.; Richins, S.; Wang, H.; Xu, W.; Rui, X.; Luo, H. Ultrafine Nb_2O_5 Nanocrystal Coating on Reduced Graphene Oxide as Anode Material for High Performance Sodium Ion Battery. *ACS Appl. Mater. Interfaces* **2016**, *8* (34), 22213−22219.
(45) Hummers, W. S.; Offeman, R. E. Preparation of Graphitic Oxide. *J. Am. Chem. Soc.* **1958**, *80* (6), 1339−1339.
(46) Zhang, X.; Zhu, J.; Tiwary, C. S.; Ma, Z.; Huang, H.; Zhang, J.; Lu, Z.; Huang, W.; Wu, Y. Palladium Nanoparticles Supported on Nitrogen and Sulfur Dual-Doped Graphene as Highly Active Electrocatalysts for Formic Acid and Methanol Oxidation. *ACS Appl. Mater. Interfaces* **2016**, *8* (17), 10858−10865.
(47) Youn, H.-C.; Jeong, J. H.; Roh, K. C.; Kim, K.-B. Graphene−Selenium Hybrid Microballs as Cathode Materials for High-Performance Lithium−Selenium Secondary Battery Applications. *Sci. Rep.* **2016**, *6*, 30865−30870.
(48) Yang, D.; Velamakanni, A.; Bozoklu, G.; Park, S.; Stoller, M.; Piner, R. D.; Stankovich, S.; Jung, I.; Field, D. A.; Ventrice, C. A.; Ruoff, R. S. Chemical Analysis of Graphene Oxide Films after Heat and Chemical Treatments by X-Ray Photoelectron and Micro-Raman Spectroscopy. *Carbon* **2009**, *47* (1), 145−152.
(49) Huang, Y.; Miao, Y.-E.; Fu, J.; Mo, S.; Wei, C.; Liu, T. Perpendicularly Oriented Few-Layer $MoSe_2$ on SnO_2 Nanotubes for Efficient Hydrogen Evolution Reaction. *J. Mater. Chem. A* **2015**, *3* (31), 16263−16271.
(50) Yannopoulos, S. N.; Andrikopoulos, K. S. Raman Scattering Study on Structural and Dynamical Features of Noncrystalline Selenium. *J. Chem. Phys.* **2004**, *121* (10), 4747−4758.
(51) Li, I. L.; Ruan, S. C.; Li, Z. M.; Zhai, J. P.; Tang, Z. K. Resonant Raman Study of Confined Se Single Helix and Se8 Rings. *Appl. Phys. Lett.* **2005**, *87* (7), 071902−071904.
(52) Wu, Y.; Xu, M.; Chen, X.; Yang, S.; Wu, H.; Pan, J.; Xiong, X. CTAB-Assisted Synthesis of Novel Ultrathin $MoSe_2$ Nanosheets Perpendicular to Graphene for the Adsorption and Photodegradation of Organic Dyes under Visible Light. *Nanoscale* **2016**, *8* (1), 440−450.
(53) Mao, J.; Yu, Y.; Wang, L.; Zhang, X.; Wang, Y.; Shao, Z.; Jie, J. Ultrafast, Broadband Photodetector Based on $MoSe_2$/Silicon Heterojunction with Vertically Standing Layered Structure Using Graphene as Transparent Electrode. *Adv. Sci.* **2016**, *3*, 1600018.
(54) Poorahong, S.; Izquierdo, R.; Siaj, M. An Efficient Porous Molybdenum Diselenide Catalyst for Electrochemical Hydrogen Generation. *J. Mater. Chem. A* **2017**, *5* (39), 20993−21001.
(55) Lei, Z.; Xu, S.; Wu, P. Ultra-Thin and Porous $MoSe_2$ Nanosheets: Facile Preparation and Enhanced Electrocatalytic Activity towards the Hydrogen Evolution Reaction. *Phys. Chem. Chem. Phys.* **2016**, *18* (1), 70−74.

DOI: 10.1021/acsanm.8b00208
ACS Appl. Nano Mater. 2018, 1, 2143−2152

(56) Wang, H.; Kong, D.; Johanes, P.; Cha, J. J.; Zheng, G.; Yan, K.; Liu, N.; Cui, Y. $MoSe_2$ and WSe_2 Nanofilms with Vertically Aligned Molecular Layers on Curved and Rough Surfaces. *Nano Lett.* **2013**, *13* (7), 3426−3433.
(57) Kong, D.; Wang, H.; Cha, J. J.; Pasta, M.; Koski, K. J.; Yao, J.; Cui, Y. Synthesis of MoS_2 and $MoSe_2$ Films with Vertically Aligned Layers. *Nano Lett.* **2013**, *13* (3), 1341−1347.
(58) Moon, I. K.; Lee, J.; Ruoff, R. S.; Lee, H. Reduced Graphene Oxide by Chemical Graphitization. *Nat. Commun.* **2010**, *1* (6), 1−6.
(59) Moudler, J. F.; Stickle, W. F.; Sobol, P. E.; Bomben, K. D. *Handbook of X-Ray Photoelectron Spectroscopy: A Reference Book of Standard Spectra for Identification and Interpretation of XPS Data*; Perkin-Elmer: Eden Prairie, MN, 1992.
(60) Flynn, N. T.; Gewirth, A. A. Synthesis and Characterization of Molybdate-Modified Platinum Nanoparticles. *Phys. Chem. Chem. Phys.* **2004**, *6* (6), 1310−1315.
(61) Fominski, V. Y.; Romanov, R. I.; Fominski, D. V.; Shelyakov, A. V. Preparation of $MoSe_{x>3}$/Mo-NPs Catalytic Films for Enhanced Hydrogen Evolution by Pulsed Laser Ablation of MoSe2 Target. *Nucl. Instrum. Methods Phys. Res., Sect. B* **2018**, *416*, 30−40.
(62) Shenasa, M.; Sainkar, S.; Lichtman, D. XPS Study of Some Selected Selenium Compounds. *J. Electron Spectrosc. Relat. Phenom.* **1986**, *40* (4), 329−337.
(63) Naveau, A.; Monteil-Rivera, F.; Guillon, E.; Dumonceau, J. Interactions of Aqueous Selenium (−II) and (IV) with Metallic Sulfide Surfaces. *Environ. Sci. Technol.* **2007**, *41* (15), 5376−5382.
(64) Sui, Z.-Y.; Meng, Y.-N.; Xiao, P.-W.; Zhao, Z.-Q.; Wei, Z.-X.; Han, B.-H. Nitrogen-Doped Graphene Aerogels as Efficient Supercapacitor Electrodes and Gas Adsorbents. *ACS Appl. Mater. Interfaces* **2015**, *7* (3), 1431−1438.
(65) Compton, O. C.; Jain, B.; Dikin, D. A.; Abouimrane, A.; Amine, K.; Nguyen, S. T. Chemically Active Reduced Graphene Oxide with Tunable C/O Ratios. *ACS Nano* **2011**, *5* (6), 4380−4391.
(66) Lee, S. Y.; Choi, C. H.; Chung, M. W.; Chung, J. H.; Woo, S. I. Dimensional Tailoring of Nitrogen-Doped Graphene for High Performance Supercapacitors. *RSC Adv.* **2016**, *6* (60), 55577−55583.
(67) Pourbaix, M. *Atlas of Electrochemical Equilibria in Aqueous Solutions*; Pergamon Press: New York, 1966.
(68) Bard, A. J.; Parsons, R.; Jordan, J.; *Standard Potentials in Aqueous Solution*; IUPAC-Marcel Dekker Inc.: New York, 1985.
(69) Iqbal, S.; Bondü, C.; Baltruschat, H. Quantitative Determination of H_2Se at Model Metal fcc(111) Selenide Surface: DEMS, STM, and AFM Studies. *J. Phys. Chem. C* **2015**, *119* (35), 20515−20523.
(70) Cabral, M. F.; Pedrosa, V. A.; Machado, S. A. S. Deposition of Selenium Thin Layers on Gold Surfaces from Sulphuric Acid Media: Studies Using Electrochemical Quartz Crystal Microbalance, Cyclic Voltammetry and AFM. *Electrochim. Acta* **2010**, *55* (3), 1184−1192.
(71) Vrubel, H.; Hu, X. Growth and Activation of an Amorphous Molybdenum Sulfide Hydrogen Evolving Catalyst. *ACS Catal.* **2013**, *3* (9), 2002−2011.
(72) Merki, D.; Fierro, S.; Vrubel, H.; Hu, X. Amorphous Molybdenum Sulfide Films as Catalysts for Electrochemical Hydrogen Production in Water. *Chem. Sci.* **2011**, *2* (7), 1262−1267.
(73) Liu, Z.; Li, N.; Zhao, H.; Du, Y. Colloidally Synthesized $MoSe_2$/graphene Hybrid Nanostructures as Efficient Electrocatalysts for Hydrogen Evolution. *J. Mater. Chem. A* **2015**, *3* (39), 19706−19710.
(74) Pham, K.-C.; Chang, Y.-H.; McPhail, D. S.; Mattevi, C.; Wee, A. T. S.; Chua, D. H. C. Amorphous Molybdenum Sulfide on Graphene−Carbon Nanotube Hybrids as Highly Active Hydrogen Evolution Reaction Catalysts. *ACS Appl. Mater. Interfaces* **2016**, *8* (9), 5961−5971.
(75) Xie, J.; Zhang, H.; Li, S.; Wang, R.; Sun, X.; Zhou, M.; Zhou, J.; Lou, X. W.; Xie, Y. Defect-Rich MoS_2 Ultrathin Nanosheets with Additional Active Edge Sites for Enhanced Electrocatalytic Hydrogen Evolution. *Adv. Mater.* **2013**, *25* (40), 5807−5813.
(76) Park, G. D.; Kim, J. H.; Park, S.-K.; Kang, Y. C. $MoSe_2$ Embedded CNT-Reduced Graphene Oxide Composite Microsphere with Superior Sodium Ion Storage and Electrocatalytic Hydrogen Evolution Performances. *ACS Appl. Mater. Interfaces* **2017**, *9* (12), 10673−10683.
(77) Zheng, Y.; Jiao, Y.; Jaroniec, M.; Qiao, S. Z. Advancing the Electrochemistry of the Hydrogen-Evolution Reaction through Combining Experiment and Theory. *Angew. Chem., Int. Ed.* **2015**, *54* (1), 52−65.
(78) Cai, Y.; Yang, X.; Liang, T.; et al. Easy Incorporation of Single-Walled Carbon Nanotubes into Two-Dimensional MoS_2 for High-PerformanceHydrogen Evolution. *Nanotechnology* **2014**, *25* (46), 465401−46506.
(79) Zhao, Y.; Lv, C.; Huang, Q.; Huang, Z.; Zhang, C. Self-Supported Tungsten/tungsten Dioxide Nanowires Array as an Efficient Electrocatalyst in the Hydrogen Evolution Reaction. *RSC Adv.* **2016**, *6* (92), 89815−89820.

DOI: 10.1021/acsanm.8b00208
ACS Appl. Nano Mater. 2018, 1, 2143−2152